Ballistic and delayed photodissociation channels in the $\tilde{B}\ 2\,^1A_1$ state of water studied with resonant inelastic x-ray scattering

Nina Ignatova,[1,*] Victor Kimberg,[1] Faris Gel'mukhanov,[1,2] Annette Pietzsch,[2] Sebastian Eckert,[2] Mattis Fondell,[2] Brian Kennedy,[2] Marcus Dantz,[3] Thorsten Schmitt,[3] Michael Odelius,[4] Alexander Föhlisch,[2,5] and Vinícius Vaz da Cruz[2,†]

[1]*KTH Royal Institute of Technology, Division of Theoretical Chemistry and Biology, SE-10691 Stockholm, Sweden*

[2]*Helmholtz-Zentrum Berlin für Materialien und Energie, Institute for Methods and Instrumentation for Synchrotron Radiation Research, Albert-Einstein-Strasse 15, D-12489 Berlin, Germany*

[3]*Photon Science Division, Paul Scherrer Institut, CH-5232 Villigen PSI, Switzerland*

[4]*Department of Physics, Stockholm University, AlbaNova University Center, SE-10691 Stockholm, Sweden*

[5]*Universität Potsdam, Institut für Physik und Astronomie, Karl-Liebknecht-Strasse 24/25 D-14476 Potsdam-Golm, Germany*

(Received 9 November 2023; revised 24 April 2024; accepted 29 July 2024; published 27 September 2024)

Photodissociation is one of the most important photoinduced chemical reactions. It occurs when the potential energy curve along a chemical bond is repulsive in an excited state. Typically, "ballistic" ultrafast dissociation leads to the broadening of absorption resonances and the smearing out of vibrational fine-structure. We report on the photodissociation of H_2O in the $\tilde{B}\ 2\ ^1A_1$ electronic state, characterized by a $|3a_1^{-1}4a_1^1\rangle$ configuration, which can be reached via resonant inelastic x-ray scattering or direct ultraviolet absorption. In both cases the spectra show narrow vibrational resonances, in spite of the dissociative character of the state. We find that "delayed" dissociation pathways, caused by reflection of the nuclear wave packet, are responsible for this effect. In spite of the analogous topology of the potential energy surfaces of the core- and valence-excited states, the reflection of the wave packet takes place only in the latter. The two-dimensional wave packet of the O-H stretching coordinates becomes trapped in a "cavity" near the Franck-Condon region, resulting from a mismatch between the OH vibrational frequency in the cavity and the one at the dissociation limit.

DOI: 10.1103/PhysRevA.110.033119

I. INTRODUCTION

The simplest model describing the dissociation of a polyatomic molecule along a given chemical bond relies on a one-dimensional (1D) potential energy curve (PEC) following the dissociation pathway. Although this picture works well for many cases studied in optical and x-ray spectroscopy [1,2], it constitutes only an idealized scenario and does not always capture the essential physics of a process. The $\tilde{B}\ 2\ ^1A_1$ of water is a prime example where the dissociative pathway is not direct and strongly affected by mode-coupling and wave-packet reflections. Among the spectroscopic tools developed to investigate the potential energy surface (PES), resonant inelastic x-ray scattering (RIXS) has emerged as a powerful technique capable of mapping nuclear dynamics in isolated molecules [3–7] and liquids [8–12]. Its main advantage being the ability to reach a desired final state indirectly, via core excitation, creating vibrational-mode-selective nuclear wave packets to probe the target PES [3,5,6].

We focus on a RIXS channel

$$H_2O(\tilde{X}\,1^1A_1) + \omega \rightarrow \left|1s^{-1}4a_1^1\right\rangle \rightarrow H_2O(\tilde{B}2^1A_1) + \omega' \rightarrow H + OH(^2\Sigma) \quad (1)$$

to the dissociative $\tilde{B}\ 2\ ^1A_1\ |3a_1^{-1}4a_1^1\rangle$ valence-excited state when the frequency of the incoming x-ray photon ω is tuned to the resonance of the lowest core-excited state $|1s^{-1}4a_1^1\rangle$ [Fig. 1(a)], which is also dissociative along the OH bonds. The decay of the core-excited state is accompanied by emission of the x-ray photon ω' [see (1) and Fig. 1(a)]. The same final state can be reached directly by the UV absorption studied earlier [13–16]. The electronic and rovibrational state distribution of the OH fragment photoproduct has also been heavily debated [17–21]. Notably, this electronic state was previously observed using low-resolution RIXS by Weinhardt *et al.* [22], where deuteration evidenced ultrafast dissociation features in the spectrum. However, their limited spectral resolution did not allow to clearly study the intricate nuclear dynamics which our measurements revealed. Supported by theoretical simulations, using three different levels of approximation for the coupling of the vibrational modes, we disclose a trapping of the nuclear wave packet along the OH stretching modes.

Previously, the effect of the bending wave packet recurrence in the $\tilde{B}\ 2\ ^1A_1$ state was discussed in connection to the UV-absorption spectra of water [15,16]. Although the coupling of a single OH stretch and the bending angle was accounted for, the coupling between the stretching modes was

*Contact author: ninai@kth.se
†Contact author: vinicius.vaz_da_cruz@helmholtz-berlin.de

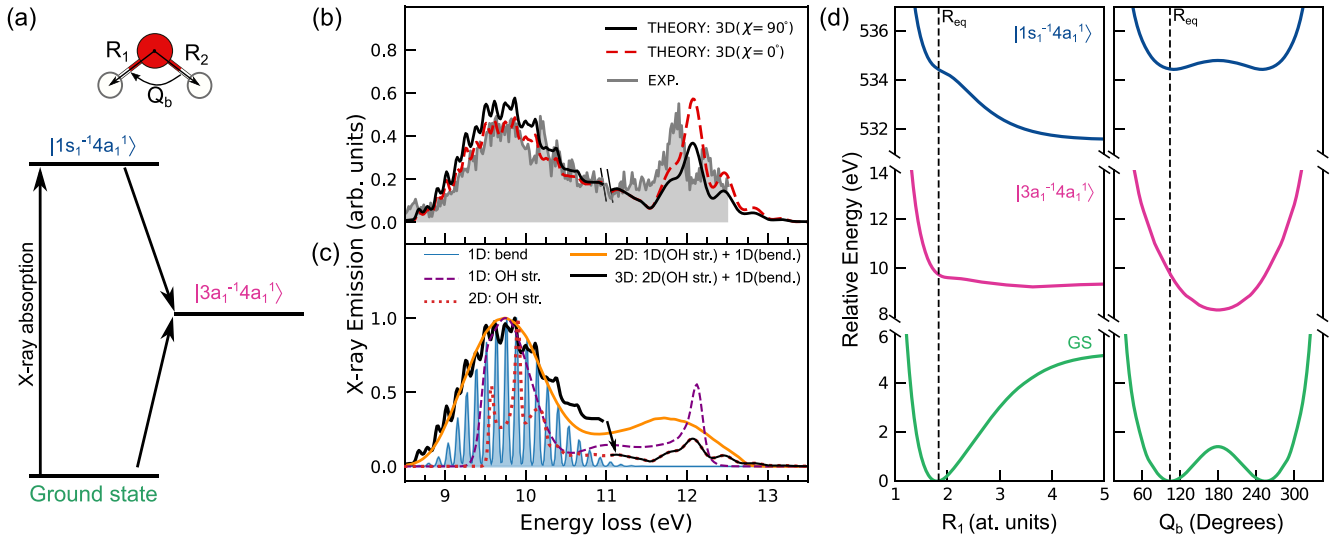

FIG. 1. (a) Energy level diagram of the electronic states involved in the RIXS process. (b) Experimental (shaded area, $\chi = 90°$) and theoretical (solid-black and dashed-red curves for $\chi = 90°$ and $0°$, respectively) RIXS spectra of H_2O as a function of energy loss, $\omega - \omega'$. (c) RIXS spectrum computed within different theoretical models; theoretical spectra are shifted by 0.3 eV towards higher energy to fit the experiment and normalized on the maximum; 3D (black) and 2D (red dashed) cross sections are matched at the maxima. (d) One-dimensional potential energy curves along the R_1 coordinate (left) and HOH angle (right) for the ground state (GS), core-excited $|1s^{-1}4a_1^1\rangle$, and final $|3a_1^{-1}4a_1^1\rangle$ states, scanned at the ground-state equilibrium geometry.

ignored. Contrary to UV absorption, which is sensitive to the Franck-Condon (FC) region, RIXS allows to prepare a specific distribution of the intermediate nuclear wave packet in the core-excited state [3,6]. This wave packet is projected on the final surface, making it possible to investigate further details of the stretching dynamics in the electronic state of interest.

In our article we focus on the unusual features of the RIXS and x-ray absorption spectra of gas phase water molecules caused by the dynamics of the two-dimensional (2D) wave packet of the coupled O-H stretching coordinates.

The article is organized as follows. In Sec. II we outline the RIXS experiment. The time-dependent theory of RIXS and absorption together with the details of simulations are given in Sec. III. The obtained results are discussed in Sec. IV. Section IV A contains our main result, namely, the dissociative broadening of x-ray absorption spectrum (XAS) and spectral narrowing of the RIXS profile. In Sec. IV B we show that the physical reason for this is the qualitatively different wave-packet propagation in core-excited and final states. Our findings are summarized in the last section, Sec. V.

II. EXPERIMENTAL RESULTS

The experimental RIXS spectrum was acquired by using the SAXES spectrometer [23] at the RIXS end station of the ADRESS beam line [24] at the Swiss Light Source, Paul Scherrer Institut. The H_2O(g) sample was prepared by evacuation and heating (60°) of a 10-ml H_2O(l) sample reservoir. The gas was transferred towards the interaction point through previously evacuated and heated steel capillaries. The sample volume was separated from the experimental chamber by a 150-nm-thick silicon nitride membrane. A continuous sample replacement was established by constant evacuation of the H_2O(l) sample reservoir thereby generating a flow of fresh sample at the interaction volume. The signal emitted from the sample volume was detected at a total scattering angle of 90°. The photon energy ω was tuned to the maximum of the $|1s^{-1}4a_1^1\rangle$ x-ray absorption resonance [25] at 534 eV. Scattered photons were detected with a combined experimental resolution of 75 meV.

The experimental and simulated RIXS spectra shown in Figs. 1(b) and 1(c), respectively, consist of two bands: one broader band, with some diffuse fine-structure, located around 9.8 eV, and another sharper band around 11.8 eV. These bands arise through qualitatively distinct mechanisms which are crucial for understanding this RIXS channel. The first band is a so-called molecular band, arising from transitions near the vertical excitation point of the surfaces, being sensitive to short-range wave packet dynamics. Meanwhile, the second band constitutes a fragment band, resulting from transitions of the core-excited wave packet in the dissociative limit, i.e., in the OH radical species [4,6]. In between the two bands, sharp peaks are observed owing to other electronic states [26].

III. DETAILS OF SIMULATIONS

Our theoretical simulations of the RIXS process utilize the time-dependent wave packet technique [6,7], that includes three models of vibrational dynamics with increasing complexity [see Fig. 1(c)] utilizing a mixed time-dependent and time-independent formalism which we will outline below.

A. Mixed time-dependent and time-independent formulation of the RIXS and absorption cross sections: 2D + 1D model

We compute the RIXS cross-section by assuming the adiabatic separation of the bending and stretching motions in the framework of the 2D + 1D model [3,7], where the 2D stretching was simulated using the time-dependent wave

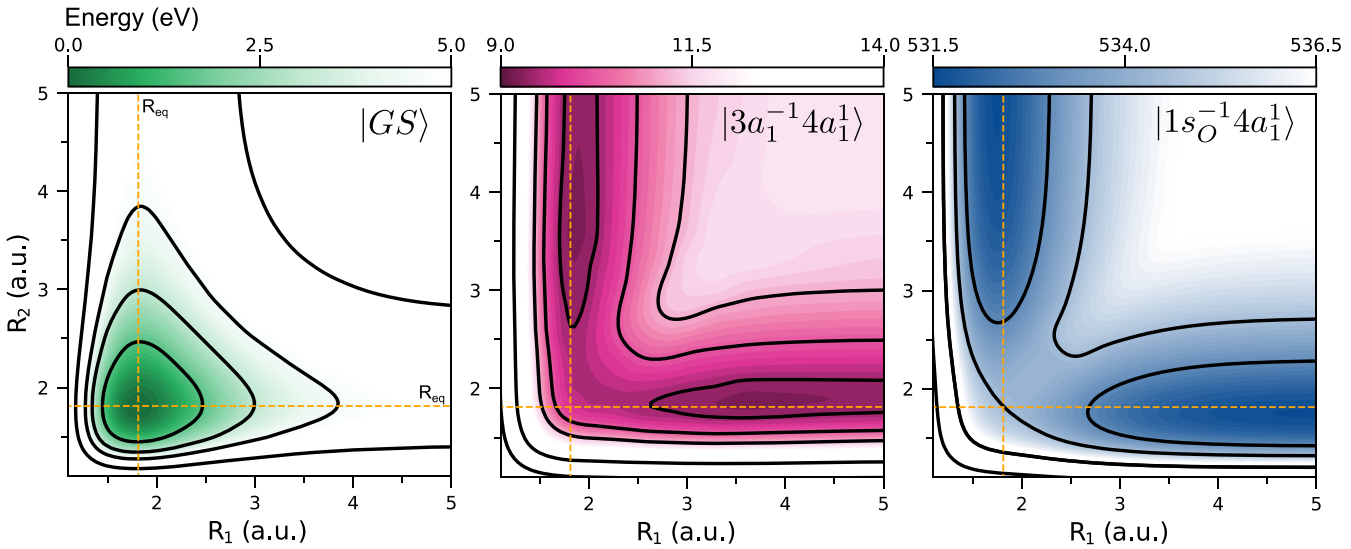

FIG. 2. Color maps of the calculated two-dimensional potential energy surfaces for the ground state, valence excited state, and core-excited state of H_2O relevant to the RIXS channel studied in this work.

packet approach while we use the stationary FC approach for the bending mode

$$\sigma^{(\mathrm{RIXS})}(\omega',\omega) = \frac{1}{\pi}\mathrm{Re}\sum_{\nu_f\nu_c'\nu_c}\langle 0|\nu_c'\rangle\langle\nu_c'|\nu_f\rangle\langle\nu_f|\nu_c\rangle\langle\nu_c|0\rangle \times\int_0^\infty dt\ \sigma_{\nu_c'\nu_c}(t)\,e^{\imath(\omega-\omega'-\omega_{f0}-\epsilon_{\nu_f}+\epsilon_0+\imath\Gamma_f)t},$$
$$\sigma_{\nu_c'\nu_c}(t) = \left\langle\Psi_{\nu_c'}(0)\middle|\Psi_{\nu_c}(t)\right\rangle,$$
$$\left|\Psi_{\nu_c}(t)\right\rangle = e^{-\imath H_f t}|\Psi_{\nu_c}(0)\rangle,$$
$$\left|\Psi_{\nu_c}(0)\right\rangle = d_{fc}(R)\int_0^\infty dt\ e^{-\imath H_c t}d_{c0}(R)|0\rangle \times e^{\imath(\omega-\omega_{c0}+\epsilon_0-\epsilon_{\nu_c}+\imath\Gamma)t}. \quad (2)$$

Here H_i is the 2D nuclear Hamiltonian of the stretching modes of the electronic state $i = c, f$, ϵ_0 is the total zero-point energy of bending and stretching modes of the ground electronic state, ϵ_{ν_i} and $|\nu_i\rangle$ are the vibration energy and corresponding wave function of the bending mode of the ith electronic state, and Γ_f and Γ are the lifetime broadenings of the final and core-excited states, respectively.

The cross section of the absorption from the ground to the ith electronic state is computed using the same 2D + 1D model

$$\sigma^{(\mathrm{abs})}(\omega) = \sum_{\nu_i}|\langle 0|\nu_i\rangle|^2\langle 0|\Psi_{\nu_i}(0)\rangle,$$
$$|\Psi_{\nu_i}(0)\rangle = \int_0^\infty dt\ e^{-\imath H_i t}d_{i0}(R)|0\rangle\ e^{\imath(\omega-\omega_{i0}+\epsilon_0-\epsilon_{\nu_i}+\imath\Gamma)t}. \quad (3)$$

B. *Ab initio* calculations of the potential energy surfaces and transition dipole moments

The 2D PESs of the stretching motion for the ground and core-excited states (Fig. 2), as well the one-dimensional (1D) bending curves [Fig. 1(d)], are taken from Ref. [3] while the respective surfaces for the $|3a_1^{-1}4a_1^1\rangle$ state [Figs. 2 and 1(d)] were computed at the RASPT2 level, described in detail below.

The potential energy surfaces and transition dipole moments were obtained from multiconfiguration quantum chemical calculations using the OpenMolcas program, version 19.11 [27]. Accounting for the coupling of two stretching modes of water, we perform a 2D scan of the PES along the coordinates corresponding to the elongation of the OH bonds, $R_1 = R(\mathrm{O\text{-}H_1})$ and $R_2 = R(\mathrm{O\text{-}H_2})$ with fixed equilibrium angle $\Theta_0 = \angle(\mathrm{H_1\text{-}O\text{-}H_2}) = 104.2^\circ$ at the ground-state equilibrium position. We also perform a single scan along the bending coordinate Θ with the bond lengths $R_1 = R_2 = R_0$ fixed at the ground-state equilibrium geometry. The calculations were performed in C_s symmetry. Ground-state geometry and normal vibrational modes are determined at the second-order complete active space perturbation theory [CASPT2(8, 9)] theory level in our previous studies [3]. For the calculation of the ground, valence-excited, and core-excited electronic states, we use the restricted active space self-consistent field (RASSCF) method [28], with subsequent correction to the energies of the electronic states with perturbation theory at the second-order perturbation theory restricted active space (RASPT2) level [29]. Scalar relativistic effects were included via the Douglas-Kroll-Hess (DKH) method [30] and use of ANO-RCC-VTZP [31] basis set with no augmentation of basis set by adding Rydberg basis as was done in previous studies [3,4].

The coordinate-dependent transition dipole moments are derived with the RASSI approach [27]. The RASSCF active space consisted of ten active electrons distributed in 14 active orbitals of different symmetry [$a'-1a_1$ (O_{1s}), $1b_2$, $2a_1$, $3a_1$, $4a_1$, $2b_2$, plus four additional orbitals and $a''-1b_1$, plus three additional orbitals]. To reach core excitations, we use the "highly excited-state scheme" (HEXS) [32] implemented in OpenMolcas, which excludes the maximum occupation in RAS1 space, where we place the O_{1s} orbital, thereby

eliminating multiple lower energy roots. Placing the O 1*s* orbital in RAS1 and freezing it at Hartree-Fock level provides a way to obtain specific core excitation. In general, our approach is similar to previous studies of first inelastic decay channel $|1b_1^{-1}4a_1^1\rangle$ [4], however, here we increase the orbital active space to describe higher valence-excited states.

IV. DISCUSSION

First, 1D propagation along either the OH stretching (magenta curve) or the HOH bending (blue curve) coordinates is computed using the 1D cuts of the PES shown in Fig. 1(d). Next, a 2D stretching model explicitly takes into account the coupling between the two OH stretching modes, already shown to be important for RIXS in water [6]. Finally, an approximate three-dimensional (3D) model is considered by supplementing the 2D stretching dynamics with the bending mode vibrational progression within the adiabatic separation approximation [3], where a 2D wave packet is propagated for the stretching motion while the bending mode is accounted for via the FC formalism. The total theoretical spectrum [black curve in Fig. 1(b)] is obtained by merging the 3D molecular band spectrum [black curve in Fig. 1(c)] with the 2D fragment band spectrum [red curve in Fig. 1(c)], assuming the same ratio of the areas of fragment and molecular bands in the 3D and 2D calculations (see the Appendix), which allows to correctly account for the vibrational structure of the fragment, that has no bending degree of freedom. Note that both experiment and theory display a fine-structure associated with the OH stretching vibration of the hydroxyl fragment.

The core- and valence-excited states of the discussed RIXS channel are dissociative along the OH stretching coordinate [Fig. 1(d)]. The stretching dynamics dominates in the core-excited state while the bending mode is almost inactive [6] [Fig. 1(d)]. However, in the valence-excited state the bending potential shows a large shift of the equilibrium angle, with a minimum at 180°. To give insight into the studied process, we compute the RIXS cross-section at different levels of approximation. Since the ultrafast dissociation dynamics in the core-excited state plays a key role in the formation of the RIXS spectrum, let us consider the nuclear dynamics and corresponding spectra neglecting, for the time being, the bending motion. Within the simplest 1D model, we obtain the intuitively expected result where the RIXS cross section is composed of an ordinary broad dissociative resonance. An analogous result is obtained for 1D simulations of the UV absorption (Fig. 3) to the same final state $|3a_1^{-1}4a_1^1\rangle$. However, there is a qualitative difference between RIXS and UV absorption, the former is strongly affected by dynamics in the intermediate state, where the breaking of the OH bond occurs within the core-hole lifetime [4]. This effect is evidenced by the fragment peak mentioned above [Fig. 1(b)], which is absent in the UV spectrum. As shown in Ref. [4], the emission transition dipole moment exhibits rotation in the course of the dissociation. This results in a dependence of the RIXS profile [Fig. 1(b)] on the angle $\chi = \angle(\mathbf{e}, \mathbf{k}')$ between the polarization vector of incident photon and the momentum $\mathbf{k}'$ of the scattered photon [4].

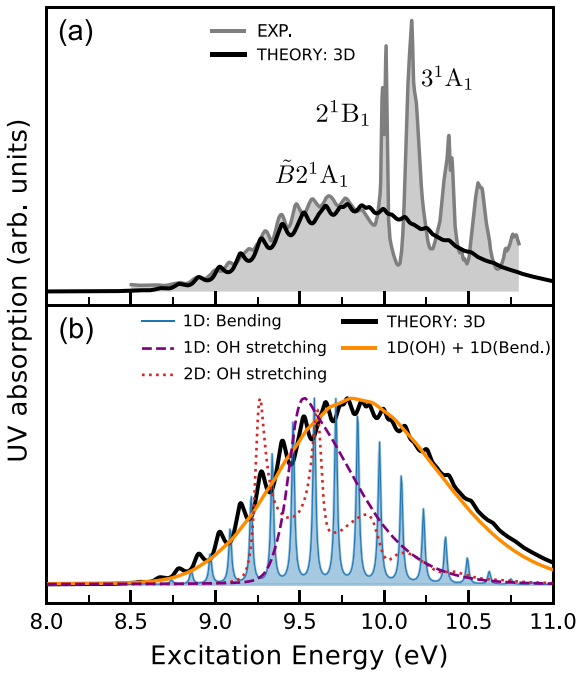

FIG. 3. (a) UV absorption spectrum [33] of gas phase H_2O in the region 8 to 11 eV compared to the theoretical simulation for the $\tilde{B}$ $2\ ^1A_1$ state, assigned to the $3a_1 \rightarrow 4a_1$ transition [26]. The sharper 2^1B_1 and $3\ ^1A_1$ bands are assigned to $1b_1 \rightarrow 5a_1$ and the $1b_1 \rightarrow 2b_1$ transitions, respectively [26]. (b) UV absorption spectra computed within various theoretical approaches.

A. Dissociative broadening versus spectral narrowing

An astonishing change of the RIXS [Fig. 1(c)] and UV absorption [Fig. 3(b)] profiles occurs when a strict wave-packet simulation is carried out using the 2D potentials for the coupled stretching coordinates [see Fig. 4(a)]. The simulations display a rather unexpected phenomenon: instead of the dissociative broadening of the molecular band the calculations display a narrowing of the RIXS and UV absorption profiles, showing clear stretching resonances [see red curves in Figs. 1(c) and 3(b)]. The observed effect stems from the dynamics of the wave packet in the 2D dissociative PESs. Since the 2D PESs for the core- and valence-excited states are very similar [Fig. 4(a)], a similar narrowing effect for x-ray absorption could be expected. However, the calculated XAS shows an opposite effect, namely, a broad dissociative $|1s^{-1}4a_1^1\rangle$ band [see insert in Fig. 4(c)], in agreement with the experimental XAS of gas-phase water showing a structureless broad dissociative profile of the first resonance $O1s \rightarrow 4a_1$ [25].

Driven by the qualitative difference between the x-ray and UV absorption profiles, we analyze the wave-packet propagation dynamics on the 2D potentials of the core- and valence-excited states. Figure 4 illustrates the dynamical origin of the spectral line narrowing of the RIXS profile. Despite the dissociative character and same topology of both core- and valence-excited state PES, the wave packets propagate very differently on these potentials. In the core-excited state, the nuclear wave packet $\psi_c(t) = e^{-\imath H_c t}|0\rangle$ propagates smoothly along the direction of the elongation of the OH bonds, referred

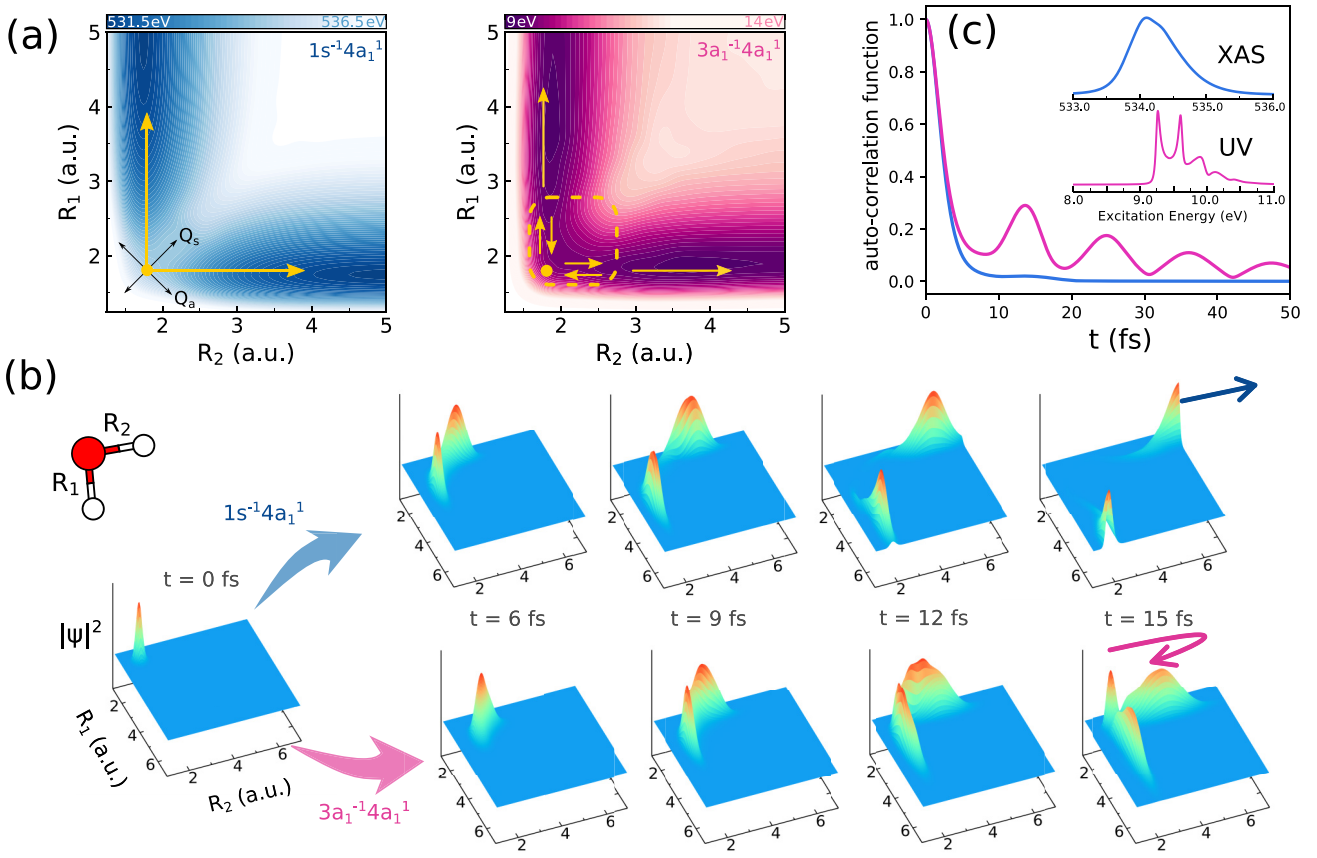

FIG. 4. (a) Two-dimensional potentials of the core-excited $|1s^{-1}4a_1^1\rangle$ and valence-excited $|3a_1^{-1}4a_1^1\rangle$ states. (b) Time evolution of the stretching wave packet on the PES of the core- and valence-excited states: direct dissociation in the core-excited state and reflection dynamics in the valence-excited state. (c) Autocorrelation function for the excitation to the core- (blue line) and valence-excited (magenta line) states; the valence-excited wave packet reflection leads to recurrences in time, while for the core-excitation only smooth decay is observed. The XAS and UV absorption spectra computed in a 2D model are displayed as inset.

to as "ballistic" dissociation. This results in an oscillation-free decay behavior of the autocorrelation function $\sigma_c(t) = \langle 0|\psi_c(t)\rangle$ of x-ray absorption [see Fig. 4(c)], which yields a single broad dissociative XAS $|1s^{-1}4a_1^1\rangle$ band. The situation is rather different for the valence-excited state $|3a_1^{-1}4a_1^1\rangle$. Although the OH bond is also dissociating, and hence there is no restoring force in that mode, we see a reflection of the wave packet $\psi_f(t) = e^{-\imath H_f t}|0\rangle$ near $R_{\rm OH} \approx 3$ a.u. causing a fraction of the wave packet to return to the FC region of the PES. This reflected part of $\psi_f(t)$ becomes temporarily trapped around the equilibrium geometry in a potential energy well, that is, leaking due to the dissociative potential, and which we for brevity will refer to as a "cavity" [see Figs. 4(b) and 4(c)]. Such confinement of the nuclear wave packet, leading to a delay of the dissociation, explains the narrowing of the stretch resonances seen in the 2D calculations of both the RIXS and UV spectra (Figs. 1 and 3). The reflected part generates recurrences (starting from $\sim$ 15 fs) in the autocorrelation function $\sigma_f(t) = \langle 0|\psi_f(t)\rangle$ [see Fig. 4(c)] resulting in narrow resonances in the energy domain [see insert in Fig. 4(c)]. The reason for the oscillatory structure in the autocorrelation function [Fig. 4(c)] is the interference between the dissociative wave packet and a reflected wave. These temporal recurrences lead to a fine-structure in the UV absorption

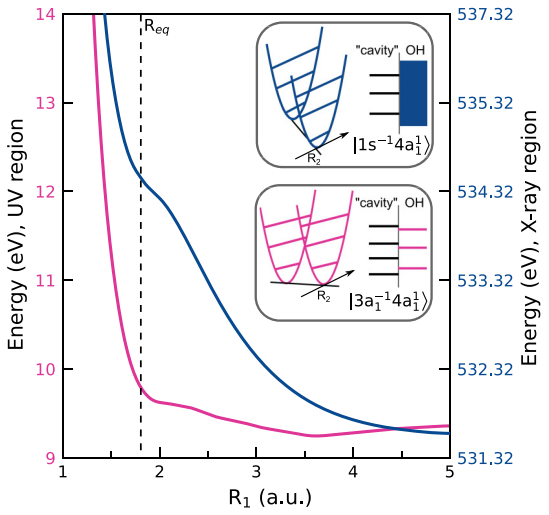

FIG. 5. Physical reasons for the reflection of the nuclear wave packet in the $|3a_1^{-1}4a_1^1\rangle$ state ($\tilde{B}\ 2\ ^1A_1$). Potential energy curves along the R_1 coordinate for core-excited (blue) and valence excited state (magenta). The less steep gradient profile of the PEC for the $\tilde{B}\ 2\ ^1A_1$ causes a mismatch of the vibrational energy levels between the symmetric stretch mode in the "cavity," near the Franck-Condon region, and the OH vibrational frequency in the dissociative limit.

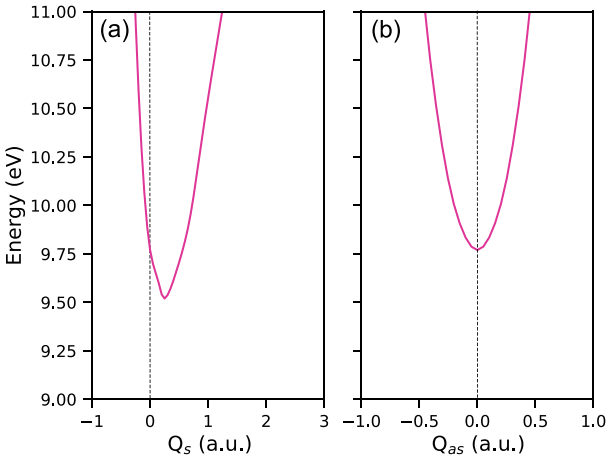

FIG. 6. One-dimensional cut of the $|3a^{-1}4a^{1}\rangle$ potential energy surface along the (a) Q_s and (b) Q_a normal coordinates.

TABLE I. Calculated OH stretching vibrational eigenvalues (E_n) for the $|3a^{-1}4a^{1}\rangle$ state obtained using a 1D cut along the ground-state symmetric stretching normal mode coordinate (Q_s). The reduced mass used was $\mu_{Q_s} = 1.0445$ amu.

n	E_n (a.u.)	E_n (eV)	E_n-E_0 (eV)
0	0.009	0.230	0.000
1	0.025	0.678	0.448
2	0.041	1.114	0.884
3	0.057	1.541	1.311
4	0.072	1.960	1.730
5	0.087	2.365	2.135
6	0.101	2.757	2.528
7	0.115	3.139	2.909
8	0.129	3.514	3.284
9	0.143	3.882	3.652
10	0.156	4.241	4.011
11	0.169	4.589	4.359

profile, in contrast to x-ray absorption where the recurrences are absent. The narrow fine-structure in the stretching spectrum enables resolution of the bending resonances in the experimental UV absorption and RIXS spectra, which dress each narrow stretching mode resonance [Figs. 1(b) and 1(c)].

B. Physical reason for ballistic and delayed wave-packet propagations

Let us now explain the reason for a ballistic propagation of the nuclear wave packet in the core-excited state $|1s^{-1}4a_1^1\rangle$ and the reflection of the wave packet in valence-excited state $|3a_1^{-1}4a_1^1\rangle$. To that end, we compare 1D cuts through the PES of the $|1s^{-1}4a_1^1\rangle$ and $|3a_1^{-1}4a_1^1\rangle$ states (see Fig. 5). One can see a qualitative difference between these 1D potentials near the equilibrium, where the "molecular" band is formed. Contrary to the core-excited state PEC, having a sufficient gradient near equilibrium $-dE_c(R)/dR$, the slope of the 1D potential of the valence-excited state is nearly zero $[-dE_f(R)/dR \approx 0]$ around the transition region from the "cavity" near the equilibrium $R = R_{\rm eq}$ to the dissociative valley. Note that the "cavity," near the equilibrium, is bound along the symmetric stretching mode, having a vibrational frequency of $\omega_{\rm sym} \approx 0.45$ eV (see Fig. 6 and Table I). The potential, and hence the frequency, changes gradually along the dissociation pathway, ultimately leading to the vibrational frequency of the OH fragment (see Figs. 7 and 8 and Table II). This intricate behavior is reflected in the asymmetry and irregularity of the stretching resonances in the 2D calculated RIXS and UV absorption spectra in Figs. 1–3 (see also Table III).

Let us focus on the transition region between the "cavity" and the dissociation valley. For the core-excited state, the OH vibrations form a continuum in this region because of the nonzero slope $-dE_c(R)/dR \neq 0$ (see Fig. 5) along the dissociative coordinate. Thus, there is a good matching between the "cavity" vibrational frequency and the continuum spectrum of the dissociative valley in the transition region (Fig. 5) and, hence, ballistic dissociation. The picture is different for the valence-excited state where the slope is nearly zero $-dE_f(R)/dR \approx 0$ in the transition region. This means that the OH vibrations do not form a continuum in this case. Since the cavity frequency $\omega_{\rm sym}$ does not match the dissociation valley frequency $\omega_{OH} = 0.38$ eV (Fig. 5), the wave packet is reflected in the transition region (Fig. 5) and the hydrogen atom transiently trapped in the cavity.

We treat the dynamics along the bending mode in the framework of the adiabatic separation of the bending and stretching motions through our 2D + 1D model [3]. Effectively, the narrow stretching resonances described above are dressed by a FC progression of the bending mode. Within this model, the bending resonances are only resolved in the spectrum due to the reflections of the 2D stretching wave packet and associated recurrences in the autocorrelation function. This mechanism applies to both RIXS and UV spectra and the model leads to good agreement with the experiment.

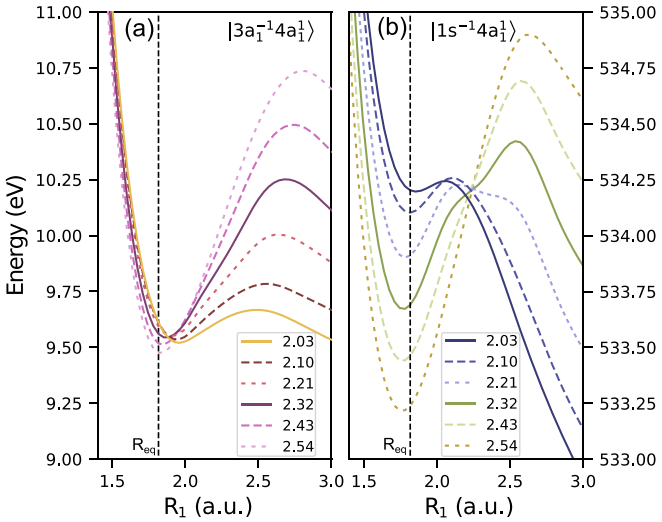

FIG. 7. One-dimensional cuts along R_1, for 2.03 a.u. $\leqslant R_2 \leqslant$ 2.54 a.u. values, through the 2D OH stretching PES of the (a) valence-excited $|3a^{-1}4a^{1}\rangle$ state and (b) core-excited $|1s_O^{-1}4a^{1}\rangle$ state. This comparison clearly shows the change in stretching frequency for the valence-excited state, in contrast with the core-excited state where the change is small.

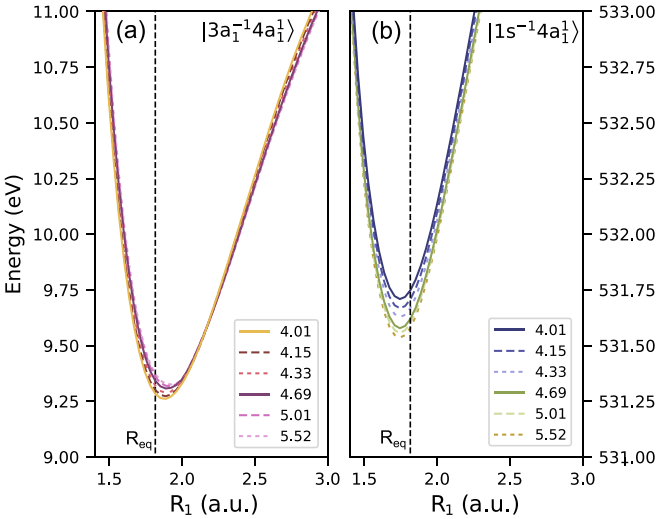

FIG. 8. One-dimensional cuts along R_1, for 4.01 a.u. $\leqslant R_2 \leqslant$ 5.52 a.u. values, through the 2D OH stretching PES of the (a) valence-excited $|3a^{-1}4a^1\rangle$ state and (b) core-excited $|1s_O^{-1}4a^1\rangle$ state. The dots show the point where the gradient is zero.

Nevertheless, it is necessary to address the fact that decoupling the bending and stretching motions constitutes a severe approximation. Weide, Kühl, and Schinke [15,16,34], as well as Segev and Shapiro [14], demonstrated the influence of the coupling of stretching and bending modes in their studies of UV absorption of water. Similarly to our model, they explain the appearance of the bending resonances in terms of coupling of two different nuclear motions and the resulting reflection of the wave packet [35] and recurrence in the autocorrelation function after about 40 fs [15]. Interestingly, both models explain the occurrence of diffuse bending resonances accompanying OH dissociation in terms of common factors: reflections of the wave packet near equilibrium caused by both coupling of the two stretching motions as well as coupling of stretching and bending modes. Thus there is a great challenge to simulate RIXS by propagating a 3D wave packet on the PES which considers coupling of all modes, as done for UV-Vis excitation [21,35] and UV-X-ray pump-probe [36]. Lastly, the approximations made in our model as well as in Weide, Kühl, and Schinke's [15,16] are complementary and reveal two important dynamical effects in the dissociation dynamics of water in the $|3a_1^{-1}4a_1^1\rangle$ state.

TABLE II. Calculated OH stretching vibrational eingevalues (E_n) for the $|3a^{-1}4a^1\rangle$ state obtained using a 1D cut along the R_1 coordinate with a R_2 fixed at the dissociative limit.

n	E_n (a.u.)	E_n (eV)	E_n-E_0 (eV)
0	0.007	0.195	0.000
1	0.021	0.575	0.380
2	0.034	0.926	0.731
3	0.046	1.254	1.059
4	0.057	1.553	1.358
5	0.067	1.823	1.628
6	0.075	2.053	1.859
7	0.082	2.233	2.038
8	0.088	2.383	2.188
9	0.091	2.465	2.270

TABLE III. Theoretical peak positions (E_n) of the RIXS energy loss and UV-Vis absorption spectra of the $|3a^{-1}4a^1\rangle$ state extracted from the 2D wave-packet simulations (without bending).

	RIXS		UV-Vis	
n	E_n (eV)	E_n-E_0 (eV)	E_n (eV)	E_n-E_0 (eV)
0	9.577	0	9.264	0
1	9.904	0.327	9.605	0.341
2	10.156	0.579	9.896	0.632
3	10.364	0.787	10.123	0.860
4	10.632	1.054	10.401	1.137

V. SUMMARY

In conclusion, we investigated experimentally and theoretically the resonant inelastic x-ray scattering of gas-phase water via the dissociative $|1s^{-1}4a_1^1\rangle$ core-excited state to the dissociative $|3a_1^{-1}4a_1^1\rangle$ final state. The scattering process is strongly affected by bond breaking in both the core-exited and valence-excited states, and the RIXS spectrum consists of a molecular and a fragment band. We observed that, unlike in other RIXS channels of water, the dissociation in the final state is not direct anymore. In contrast to the ballistic dissociation in core-excited state, the two-dimensional wave packet experiences a reflection in the stretching potential energy surface of the $\tilde{B}\ 2\ ^1A_1$ final dissociative state. Contrary to previous studies, we showed that the coupling of modes was not enough for the reflection of the wave packet. Indeed, in spite of the analogous topology of the PESs of the core-excited and final states, this reflection takes place only in the final one. The reason for this reflection was a mismatch of the vibrational frequencies in the "cavity" near the equilibrium and in the dissociation valley caused by the nearly vanishing slope of the dissociative potential near the equilibrium.

Such confinement of the wave-packet in the FC region results in a drastic narrowing of the dissociative OH stretching spectrum enabling the bending fine structure to be resolved. We expect that future high-resolution RIXS measurements will be decisive in further elucidating ballistic and delayed photodissociation channels in other systems.

ACKNOWLEDGMENTS

S.E. and A.F. acknowledge funding from the ERC-ADG-2014 - Advanced Investigator Grant No. 669531 EDAX under the Horizon 2020 EU Framework Programme for Research and Innovation. The measurements were performed at the SAXES instrument of the Swiss Light Source of the Paul Scherrer Institute in Villigen, Switzerland. V.K. acknowledges financial support from the Swedish Research Council (Grant No. 2019-03470) and STINT Mobility Grants for Internationalisation (Project No. MG2021-9085). M.O. acknowledges funding from the Swedish Research Council (VR Contract No. 2021-04521). The computations were enabled by

resources provided by the National Academic Infrastructure for Supercomputing in Sweden (NAISS) and the Swedish National Infrastructure for Computing (SNIC) at PDC and NSC partially funded by the Swedish Research Council through Grants No. 2022-06725 and No. 2018-05973.

APPENDIX: MATCHING OF THE MOLECULAR AND FRAGMENT BANDS

As it was stressed in the main text, the total theoretical RIXS spectrum [black curve in Fig. 1(b) of the main text]

$$\sigma(\omega',\omega) = \sigma^{(3D)}_{mol}(\omega',\omega) + \tilde{\sigma}^{(3D)}_{fragm}(\omega',\omega),$$
$$\tilde{\sigma}^{(3D)}_{fragm}(\omega',\omega) = \kappa\sigma^{(2D)}_{fragm}(\omega',\omega), \tag{A1}$$

is obtained by merging the 3D molecular band spectrum $\sigma^{(3D)}_{mol}(\omega',\omega)$ [black curve in Fig. 1(c)] with the 2D fragment band spectrum $\sigma^{(2D)}_{fragm}(\omega',\omega)$ [red curve in Fig. 1(c)], which allowed us to correctly account for the vibrational structure of the fragment that has no bending degree of freedom. We find the unknown merging coefficient κ taking into account that the ratio of the areas of fragment and molecular bands should be preserved

$$\frac{\tilde{S}^{(3D)}_{fragm}(\omega)}{S^{(3D)}_{mol}(\omega)} = \frac{S^{(2D)}_{fragm}(\omega)}{S^{(2D)}_{mol}(\omega)}, \tag{A2}$$

where the areas are defined by the following equations:

$$\tilde{S}^{(3D)}_{mol}(\omega) = \int \tilde{\sigma}^{(3D)}_{mol}(\omega',\omega)d\omega' = \kappa S^{(2D)}_{fragm}(\omega),$$
$$S^{(nD)}_{fragm}(\omega) = \int \tilde{\sigma}^{(nD)}_{fragm}(\omega',\omega)d\omega',$$
$$S^{(nD)}_{mol}(\omega) = \int \tilde{\sigma}^{(nD)}_{mol}(\omega',\omega)d\omega'. \tag{A3}$$

Comparing Eqs. (A2) and (A3) we get finally from Eq. (A1)

$$\sigma(\omega',\omega) = \sigma^{(3D)}_{mol}(\omega',\omega) + \kappa\sigma^{(2D)}_{fragm}(\omega',\omega), \quad \kappa = \frac{S^{(3D)}_{mol}(\omega)}{S^{(2D)}_{mol}(\omega)}. \tag{A4}$$

[1] F. Gel'mukhanov and H. Ågren, Phys. Rep. **312**, 87 (1999).
[2] F. Gel'mukhanov, M. Odelius, S. P. Polyutov, A. Föhlisch, and V. Kimberg, Rev. Mod. Phys. **93**, 035001 (2021).
[3] R. C. Couto, V. Vaz da Cruz, E. Ertan, S. Eckert, M. Fondell, M. Dantz, B. Kennedy, T. Schmitt, A. Pietzsch, F. F. Guimarães, H. Ågren, F. Gel'mukhanov, M. Odelius, V. Kimberg, and A. Föhlisch, Nat. Commun. **8**, 14165 (2017).
[4] E. Ertan, V. Savchenko, N. Ignatova, V. Vaz da Cruz, R. C. Couto, S. Eckert, M. Fondell, M. Dantz, B. Kennedy, T. Schmitt, A. Pietzsch, A. Föhlisch, F. Gel'mukhanov, M. Odelius, and V. Kimberg, Phys. Chem. Chem. Phys. **20**, 14384 (2018).
[5] S. Eckert, V. Vaz da Cruz, F. Gel'mukhanov, E. Ertan, N. Ignatova, R. C. Couto, S. Polyutov, M. Fondell, M. Dantz, B. Kennedy, T. Schmitt, A. Pietzsch, M. Odelius, and A. Föhlisch, Phys. Rev. A **97**, 053410 (2018).
[6] V. Vaz da Cruz, E. Ertan, R. C. Couto, S. Eckert, M. Fondell, M. Dantz, B. Kennedy, T. Schmitt, A. Pietzsch, F. F. Guimarães, H. Ågren, F. Gel'mukhanov, M. Odelius, A. Föhlisch, and V. Kimberg, Phys. Chem. Chem. Phys. **19**, 19573 (2017).
[7] V. Vaz da Cruz, N. Ignatova, R. C. Couto, D. A. Fedotov, D. R. Rehn, V. Savchenko, P. Norman, H. Ågren, S. Polyutov, J. Niskanen *et al.*, J. Chem. Phys. **150**, 234301 (2019).
[8] V. Savchenko, V. Ekholm, I. E. Brumboiu, P. Norman, A. Pietzsch, A. Föhlisch, J. Rubensson, J. Gråsjö, O. Björneholm, C. Såthe, M. Dong, T. Schmitt, D. McNally, X. Lu, P. Krasnov, S. P. Polyutov, F. Gel'mukhanov, M. Odelius, and V. Kimberg, J. Chem. Phys. **154**, 214304 (2021).
[9] V. Savchenko, I. E. Brumboiu, V. Kimberg, M. Odelius, P. Krasnov, J.-C. Liu, J.-E. Rubensson, O. Björneholm, C. Såthe, J. Gråsjö, M. Dong, A. Pietzsch, A. Föhlisch, T. Schmitt, D. McNally, X. Lu, S. P. Polyutov, P. Norman, M. Iannuzzi, F. Gel'mukhanov *et al.*, Sci. Rep. **11**, 4098 (2021).
[10] V. Vaz da Cruz, F. Gel'mukhanov, S. Eckert, M. Iannuzzi, E. Ertan, A. Pietzsch, R. C. Couto, J. Niskanen, M. Fondell, M. Dantz, T. Schmitt, X. Lu, D. McNally, R. M. Jay, V. Kimberg, A. Föhlisch, and M. Odelius, Nat. Commun. **10**, 1013 (2019).
[11] M. Blum, M. Odelius, L. Weinhardt, S. Pookpanratana, M. Bär, Y. Zhang, O. Fuchs, W. Yang, E. Umbach, and C. Heske, J. Phys. Chem. B **116**, 13757 (2012).
[12] O. Fuchs, M. Zharnikov, L. Weinhardt, M. Blum, M. Weigand, Y. Zubavichus, M. Bär, F. Maier, J. D. Denlinger, C. Heske, M. Grunze, and E. Umbach, Phys. Rev. Lett. **100**, 027801 (2008).
[13] H. Wang, W. S. Felps, and S. P. McGlynn, J. Chem. Phys. **67**, 2614 (1977).
[14] E. Segev and M. Shapiro, J. Chem. Phys. **77**, 5604 (1982).
[15] K. Weide, K. Kuehl, and R. Schinke, J. Chem. Phys **91**, 3999 (1989).
[16] K. Weide and R. Schinke, J. Chem. Phys. **90**, 7150 (1989).
[17] K. Weide and R. Schinke, J. Chem. Phys. **87**, 4627 (1987).
[18] D. Mordaunt, M. Ashfold, and R. Dixon, J. Chem. Phys. **100**, 7360 (1994).
[19] R. Dixon, D. Hwang, X. Yang, S. Harich, J. Lin, and X. Yang, Science **285**, 1249 (1999).
[20] K. Yuan, R. N. Dixon, and X. Yang, Acc. Chem. Res. **44**, 369 (2011).
[21] R. van Harrevelt and M. C. van Hemert, J. Chem. Phys. **112**, 5787 (2000).
[22] L. Weinhardt, A. Benkert, F. Meyer, M. Blum, R. G. Wilks, W. Yang, M. Bär, F. Reinert, and C. Heske, J. Chem. Phys. **136**, 144311 (2012).
[23] G. Ghiringhelli, A. Piazzalunga, C. Dallera, G. Trezzi, L. Braicovich, T. Schmitt, V. N. Strocov, R. Betemps, and L. Pattley, Rev. Sci. Instrum. **77**, 113108 (2006).
[24] V. N. Strocov, T. Schmitt, U. Flechsig, T. Schmidt, A. Imhof, Q. Chen, J. Raabe, R. Betemps, D. Zimoch, J. Krempasky, X. Wang, M. Grioni, A. Piazzalungaa, and L. Pattheya, J. Synchrotron Radiat. **17**, 631 (2010).
[25] A. Hiraya, K. Nobusada, M. Simon, K. Okada, T. Tokushima, Y. Senba, H. Yoshida, K. Kamimori, H. Okumura, Y. Shimizu,

A.-L. Thomas, P. Millie, I. Koyano, and K. Ueda, Phys. Rev. A **63**, 042705 (2001).
[26] C. G. Elles, C. A. Rivera, Y. Zhang, P. A. Pieniazek, and S. E. Bradforth, J. Chem. Phys **130**, 084501 (2009).
[27] I. F. Galvan, M. Vacher, A. Alavi, C. Angeli, F. Aquilante, J. Autschbach, J. J. Bao, S. I. Bokarev, N. A. Bogdanov, R. K. Carlson *et al.*, J. Chem. Theory Comput. **15**, 5925 (2019).
[28] P. Å. Malmqvist, B. O. Roos, and B. Schimmelpfennig, Chem. Phys. Lett. **357**, 230 (2002).
[29] P. Å. Malmqvist, K. Pierloot, A. R. M. Shahi, C. J. Cramer, and L. Gagliardi, J. Chem. Phys. **128**, 204109 (2008).
[30] M. Douglas and N. M. Kroll, Ann. Phys. (NY) **82**, 89 (1974).
[31] P.-O. Widmark, P. Malmqvist, and B. O. Roos, Theor. Chim. Acta **77**, 291 (1990).
[32] F. Aquilante, J. Autschbach, A. Baiardi, S. Battaglia, V. A. Borin, L. F. Chibotaru, I. Conti, L. De Vico, M. Delcey, I. F. Galván *et al.*, J. Chem. Phys **152**, 214117 (2020).
[33] R. Mota, R. Parafita, A. Giuliani, M.-J. Hubin-Franskin, J. M. C. Lourenco, G. Garcia, S. V. Hoffmann, N. J. Mason, P. A. Ribeiro, M. Raposo, and P. Limão-Vieira, Chem. Phys. Lett. **416**, 152 (2005).
[34] R. Schinke, *Photodissociation Dynamics* (Cambridge University Press, Cambridge, England, 1993).
[35] M. von Dirke, B. Heumann, K. Kühl, T. Schröder, and R. Schinke, J. Chem. Phys. **101**, 2051 (1994).
[36] C. Wang, M. Gong, Y. Cheng, V. Kimberg, X.-J. Liu, O. Vendrell, K. Ueda, and S. B. Zhang, J. Phys. Chem. Lett. **14**, 5475 (2023).